Article

Observation of the antimatter hypernucleus ${}^{4}_{\Lambda}\overline{\mathrm{H}}$

https://doi.org/10.1038/s41586-024-07823-0

Received: 20 October 2023

Accepted: 12 July 2024

Published online: 21 August 2024

Check for updates

STAR Collaboration*✉

At the origin of the Universe, an asymmetry between the amount of created matter and antimatter led to the matter-dominated Universe as we know it today. The origins of this asymmetry remain unknown so far. High-energy nuclear collisions create conditions similar to the Universe microseconds after the Big Bang, with comparable amounts of matter and antimatter[1–6]. Much of the created antimatter escapes the rapidly expanding fireball without annihilating, making such collisions an effective experimental tool to create heavy antimatter nuclear objects and to study their properties[7–14], hoping to shed some light on the existing questions on the asymmetry between matter and antimatter. Here we report the observation of the antimatter hypernucleus ${}^{4}_{\Lambda}\overline{\mathrm{H}}$, composed of a $\overline{\Lambda}$, an antiproton and two antineutrons. The discovery was made through its two-body decay after production in ultrarelativistic heavy-ion collisions by the STAR experiment at the Relativistic Heavy Ion Collider[15,16]. In total, 15.6 candidate ${}^{4}_{\Lambda}\overline{\mathrm{H}}$ antimatter hypernuclei are obtained with an estimated background count of 6.4. The lifetimes of the antihypernuclei ${}^{3}_{\Lambda}\overline{\mathrm{H}}$ and ${}^{4}_{\Lambda}\overline{\mathrm{H}}$ are measured and compared with the lifetimes of their corresponding hypernuclei, testing the symmetry between matter and antimatter. Various production yield ratios among (anti)hypernuclei (hypernuclei and/or antihypernuclei) and (anti)nuclei (nuclei and/or antinuclei) are also measured and compared with theoretical model predictions, shedding light on their production mechanisms.

In 1928, Paul Dirac found possible solutions with positive and negative energies to his eponymous equation that describes the relativistic quantum behaviour of the electron[17]. It was realized in the following years that the negative-energy solution indicates a new particle with the same mass as an electron, but with opposite charge[18]. This new particle was discovered by Carl Anderson in cosmic rays in 1932 and was named the positron[19]. This established the theoretical framework and the experimental foundation for the study of antimatter. Since then, discovering new, heavier and more complicated antimatter particles and studying their properties have been an important means to explore nature. Figure 1 shows the masses compared with the years of discovery of a series of antimatter particles[7,8,19–26]. Among them, ${}^{4}_{\Lambda}\overline{\mathrm{H}}$, the discovery of which is described in this paper, is the heaviest antimatter hypernuclear cluster observed until now.

Antimatter readily annihilates with matter, making it difficult to observe antimatter nuclear clusters in the Universe. However, relativistic heavy-ion collisions can create the quark–gluon plasma state that existed in the first few microseconds of the Universe after the Big Bang, with nearly equal amounts of matter and antimatter[1–6]. The collision system expands and cools rapidly, allowing some antimatter to decouple from matter. This makes heavy-ion collisions an effective tool to create and study antimatter nuclei or hypernuclei[9–14].

There are six flavours of quarks, which belong to a group of the most basic building blocks of the visible Universe in the standard model of particle physics. Among them, the lightest up and down quarks constitute nucleons (that is, protons and neutrons) in atomic nuclei. The strange quark is the third lightest quark. Particles with strange quarks tend to decay because of the weak interaction, making strange quarks much rarer in nature than the up and down quarks. A baryon containing at least one strange quark is called a hyperon. For example, the Λ hyperon consists of an up, a down and a strange quark. Like nucleons forming an atomic nucleus, hyperons and nucleons can also constitute a bound state, called hypernucleus.

In this paper, the Solenoidal Tracker at RHIC (STAR) Collaboration[15] at the Relativistic Heavy Ion Collider (RHIC)[16] reports one of the first observations of the antimatter hypernucleus ${}^{4}_{\Lambda}\overline{\mathrm{H}}$, composed of an $\overline{\Lambda}$, an antiproton and two antineutrons. We also report the measurements of ${}^{3}_{\Lambda}\mathrm{H}$, ${}^{4}_{\Lambda}\mathrm{H}$, ${}^{3}_{\Lambda}\overline{\mathrm{H}}$ and ${}^{4}_{\Lambda}\overline{\mathrm{H}}$ decay lifetimes, and test matter–antimatter symmetry by hypernucleus–antihypernucleus lifetime comparisons. Various production yield ratios among (anti)hypernuclei (hypernuclei and/or antihypernuclei) and (anti)nuclei (nuclei and/or antinuclei) are measured and compared with the theoretical model predictions, shedding light on the production mechanism of (anti)hypernuclei in relativistic heavy-ion collisions.

(Anti)hypernucleus reconstruction

RHIC is a gigantic ring-shaped accelerator with a circumference of 3.8 km. It can accelerate heavy ions (atomic nuclei) to 99.996% of the speed of light. Pairs of these high-energy heavy ions collide, each

*A list of authors and their affiliations appears at the end of the paper. ✉e-mail: star-publication@bnl.gov

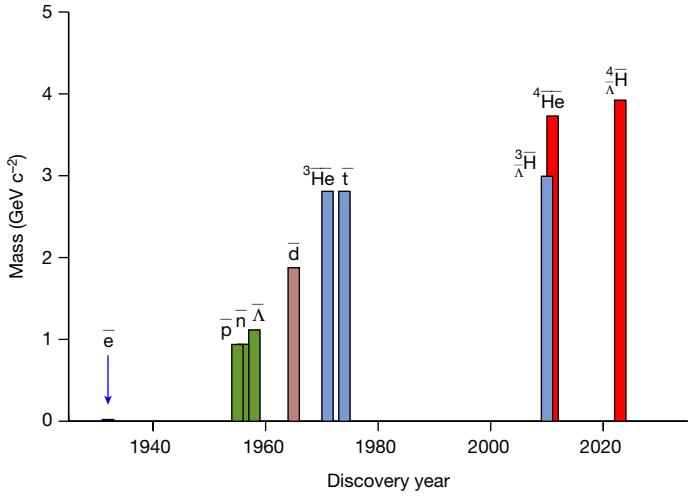

Fig. 1 | Masses versus discovery years of selected antimatter particles. The positron, antinucleons, $\bar{\Lambda}$ and antimatter (hyper)nuclear clusters are included.

producing thousands of final-state particles. The STAR experimental setup detects and records the produced particles, similar to a high-speed three-dimensional camera. More than 1,000 collisions can be recorded by STAR within a second. A total of about 6.4 billion U + U, Au + Au, Ru + Ru and Zr + Zr collision events with centre-of-mass energy per colliding nucleon–nucleon pair $\sqrt{s_{\mathrm{NN}}}$ = 193 GeV(U + U) or 200 GeV (other systems) are used in this analysis.

After being created at the collision point, (anti)hypernuclei usually fly only a distance of several centimetres before they decay. Therefore, they cannot be seen directly by the main tracking detector of STAR, the cylindrical Time Projection Chamber (TPC), which surrounds the collision point with an inner radius of about 60 cm. Instead, the (anti)hypernucleus is reconstructed by tracing back the tracks of its charged daughters to an intersection point at which the decay happened. In this analysis, the two-body decay channels $^{3}_{\Lambda}\mathrm{H} \to {}^{3}\mathrm{He} + \pi^{-}$, $^{3}_{\bar{\Lambda}}\bar{\mathrm{H}} \to {}^{3}\bar{\mathrm{He}} + \pi^{+}$, $^{4}_{\Lambda}\mathrm{H} \to {}^{4}\mathrm{He} + \pi^{-}$ and $^{4}_{\bar{\Lambda}}\bar{\mathrm{H}} \to {}^{4}\bar{\mathrm{He}} + \pi^{+}$ are used for (anti)hypernucleus reconstruction. The charged daughter particles fly out through the TPC, leaving their detectable tracks by losing energy and ionizing the gas. The TPC is placed in a 0.5-T solenoidal magnetic field, and the rigidity (momentum over charge) of the charged particle tracks can be measured from their bending in the magnetic field. Particles with different mass and electrical charge have different average ionization energy loss $\langle \mathrm{d}E/\mathrm{d}x \rangle$ compared with rigidity (Fig. 2a), which is used to identify different particles. Particle identification is further performed with the help of the Time-of-Flight (TOF) detector. The squared mass (m) over charge (Z) ratio of a particle, m^2/Z^2, is calculated from the rigidity, track length and TOF. Figure 2b,c shows $n_\sigma(^4\mathrm{He})$ and $n_\sigma(^4\bar{\mathrm{He}})$ versus m^2/Z^2, for the selection of ^{4}He and $^4\bar{\mathrm{He}}$ candidates. Here n_σ is the deviation of the measured $\langle \mathrm{d}E/\mathrm{d}x \rangle$ from the expected value for a certain particle species normalized by the resolution $\sigma_{\mathrm{d}E/\mathrm{d}x}$,

$$n_\sigma = \ln\left(\frac{\langle \mathrm{d}E/\mathrm{d}x \rangle}{\langle \mathrm{d}E/\mathrm{d}x \rangle_{\mathrm{th}}}\right)/\sigma_{\mathrm{d}E/\mathrm{d}x}. \quad (1)$$

(Anti)hypernucleus candidates are reconstructed from pairs of selected (anti)helium and $\pi^{\pm}$ tracks. To suppress background from random combinations of particles emitted from the collision point, selections have been applied such that the tracks of the two daughter particles are likely to come from a common decay vertex displaced from the collision point. The selection cuts on the topological variables are optimized for the best $^{3}_{\Lambda}\bar{\mathrm{H}}$ signal.

Signals

To observe the (anti)hypernucleus signals, the invariant mass of their daughter-pair candidates is calculated. The invariant mass is the total energy of the daughter particles in their centre-of-mass frame, calculated from their three-dimensional momenta and masses. According to energy–momentum conservation and Einstein's mass-energy equivalence, the invariant mass of the decay daughters should be equal to the parent-particle mass. The invariant-mass spectra of reconstructed $^{3}_{\Lambda}\mathrm{H}$, $^{3}_{\bar{\Lambda}}\bar{\mathrm{H}}$, $^{4}_{\Lambda}\mathrm{H}$ and $^{4}_{\bar{\Lambda}}\bar{\mathrm{H}}$ candidates are shown in Fig. 3. The narrow peaks at the (anti)hypernucleus mass positions are the (anti)hypernucleus decay signals, whereas the smooth components below are the combinatorial backgrounds. The combinatorial background invariant-mass distributions are reproduced with a rotation method, in which the (anti)helium nucleus track is randomly rotated around the beamline, so that the decay kinematics of the real signal candidate are destroyed and randomized as the combinatorial background. The final signal count N_{Sig} is extracted by subtracting the integrated combinatorial background count N_{Bg} from the integral of the signal-candidate distribution in the shaded invariant-mass region in Fig. 3.

In total, 941 ± 59 $^{3}_{\Lambda}\mathrm{H}$, 637 ± 49 $^{3}_{\bar{\Lambda}}\bar{\mathrm{H}}$, 24.4 ± 6.1 $^{4}_{\Lambda}\mathrm{H}$ and 15.6 ± 4.7 $^{4}_{\bar{\Lambda}}\bar{\mathrm{H}}$ signal candidates are observed. The significances are calculated as

$$Z_{\mathrm{count}} = \sqrt{2\left[(N_{\mathrm{Sig}} + N_{\mathrm{Bg}})\ln\left(1 + \frac{N_{\mathrm{Sig}}}{N_{\mathrm{Bg}}}\right) - N_{\mathrm{Sig}}\right]}. \quad (2)$$

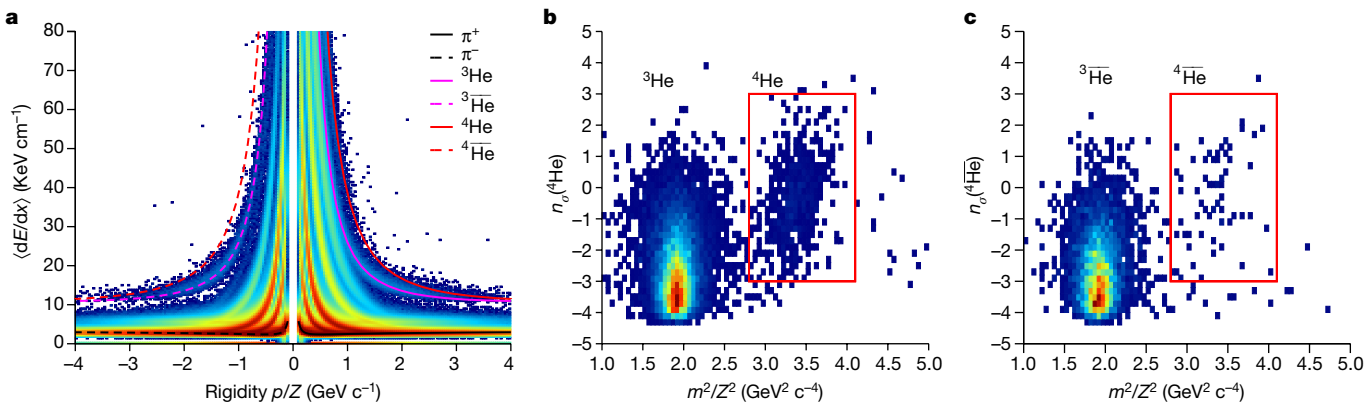

Fig. 2 | Particle identification based on energy loss and m^2/Z^2. a, Average energy loss $\langle \mathrm{d}E/\mathrm{d}x \rangle$ versus rigidity of charged particles measured by the TPC. The lines represent the expected trends for π^{+}, ^{3}He and ^{4}He and their corresponding antiparticles. **b**,**c**, $n_\sigma(^4\mathrm{He})$ (**b**) and $n_\sigma(^4\bar{\mathrm{He}})$ (**c**) versus m^2/Z^2. The red boxes indicate the region for ^{4}He and $^4\bar{\mathrm{He}}$ candidates.

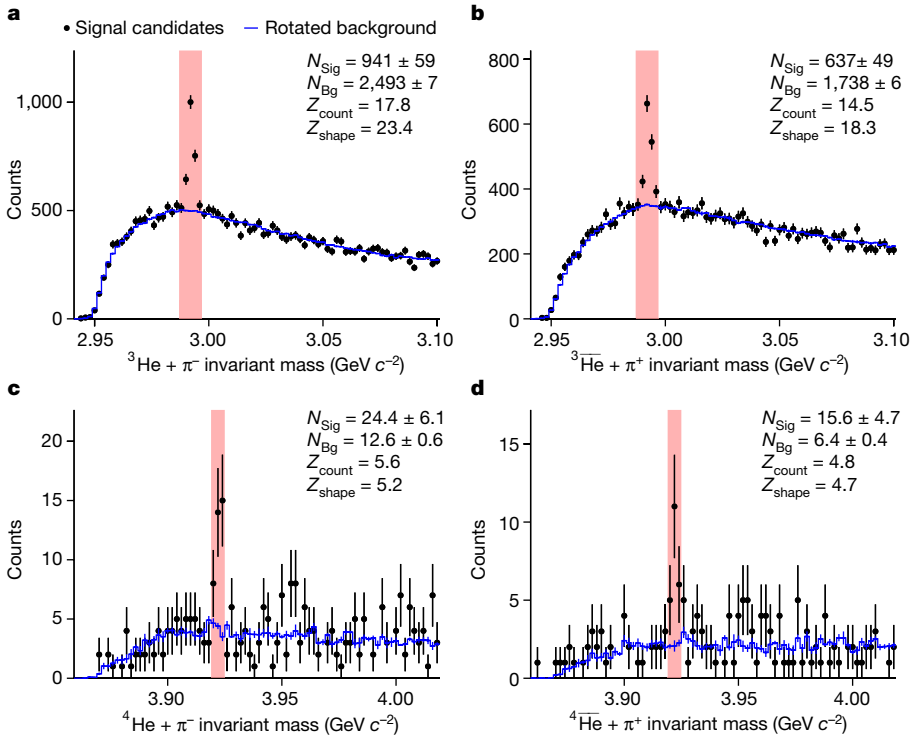

Fig. 3 | Invariant-mass distributions. a–d, Invariant-mass distributions of ^{3}He + π$^-$ (**a**), $^3\overline{\text{He}}$ + π$^+$ (**b**), ^{4}He + π$^-$ (**c**) and $^4\overline{\text{He}}$ + π$^+$ (**d**). The solid bands mark the signal invariant-mass regions. The obtained signal count (N_{Sig}), background count (N_{Bg}) and signal significances (Z_{count} and Z_{shape}) are shown in each panel.

The significances Z_{count} of ${}^4_\Lambda$H, and ${}^4_{\bar{\Lambda}}\overline{\text{H}}$ signals are 5.6 and 4.8 standard deviations (σ), corresponding to P values of 1.1×10^{-8} and 7.9×10^{-7}, respectively. The significances are also calculated by comparing the likelihoods of fitting the candidate invariant-mass distributions with a Gaussian-shaped signal plus background with the likelihoods with the hypothesis of pure background. The significances Z_{shape} are obtained as 5.2σ and 4.7σ for ${}^4_\Lambda$H and ${}^4_{\bar{\Lambda}}\overline{\text{H}}$, respectively.

Lifetimes and matter–antimatter symmetry test

Our current knowledge of physics principles suggests that the initial Universe should have contained equal amounts of matter and antimatter. However, the antiproton flux in cosmic rays and other measurements[27] indicate that no large-scale antimatter exists in the vicinity of our galaxy, and the visible Universe is almost entirely matter. We may ask where the antimatter is, and what causes this matter–antimatter asymmetry in the Universe. We expect a matter particle and its corresponding antimatter particle to have the same properties according to the *CPT* theorem, which states that physical laws should remain unchanged under the combined operation of charge conjugation C, parity transformation P and time reversal T. Comparing the properties such as mass and lifetime of a particle and its corresponding antiparticle is an important experimental way to test the *CPT* symmetry and to search for mechanisms that cause matter and antimatter asymmetry in the Universe. Recently, the ALICE[13] and STAR[10] experiments reported that there is no significant mass (binding energy) difference between deuteron and antideuteron[13], between ^{3}He and $^3\overline{\text{He}}$ (ref. 13) and between ${}^3_\Lambda$H and ${}^3_{\bar{\Lambda}}\overline{\text{H}}$ (ref. 10). ALICE has also measured the relative difference between ${}^3_\Lambda$H and ${}^3_{\bar{\Lambda}}\overline{\text{H}}$ lifetimes, which is consistent with zero (ref. 28).

Hypernucleus lifetimes are also an important tool for studying the interactions between the hyperons and nucleons within them[29], which is a vital nuclear physics input for understanding the inner structure of compact stellar objects such as neutron stars[30]. Numerous measurements[11,31–40] show slightly shorter average lifetimes of ${}^3_\Lambda$H and ${}^4_\Lambda$H than that of the Λ hyperon. The combined lifetime of ${}^3_\Lambda$H and ${}^3_{\bar{\Lambda}}\overline{\text{H}}$ has also been measured[7,28,38,41].

In this study, the lifetimes of the (anti)hypernuclei ${}^3_\Lambda$H, ${}^4_\Lambda$H, ${}^3_{\bar{\Lambda}}\overline{\text{H}}$ and ${}^4_{\bar{\Lambda}}\overline{\text{H}}$ are measured. (Anti)hypernucleus signal yields in $ct = L/\beta\gamma = L/(p/m)$ intervals are obtained as described in the section above, where c represents the speed of light, t the decay time in the (anti)hypernucleus rest frame, L the measured decay length, β the ratio of velocity to c, γ the Lorentz factor of relativistic time dilation, p the measured momentum and m the (anti)hypernucleus nominal mass. The reconstruction efficiencies of ${}^3_\Lambda$H, ${}^3_{\bar{\Lambda}}\overline{\text{H}}$, ${}^4_\Lambda$H and ${}^4_{\bar{\Lambda}}\overline{\text{H}}$ in each $L/\beta\gamma$ bin are evaluated by a Monte Carlo method in which (anti)hypernuclei are simulated using the GEANT3 software package and embedded in real collision events. In this way, the simulated (anti)hypernuclei are reconstructed in a realistic environment. Efficiency-corrected yields of ${}^3_\Lambda$H, ${}^3_{\bar{\Lambda}}\overline{\text{H}}$, ${}^4_\Lambda$H and ${}^4_{\bar{\Lambda}}\overline{\text{H}}$ as a function of $L/\beta\gamma$ are shown in Fig. 4a. The lifetimes τ are extracted by fitting the data with the exponential decay law $N(t) = N_0\exp(-t/\tau) = N_0\exp(-(L/\beta\gamma)/c\tau)$.

The extracted lifetimes are

$$\tau\left({}^3_\Lambda\text{H}\right) = 254 \pm 28(\text{stat.}) \pm 14(\text{sys.})\ \text{ps},$$
$$\tau\left({}^3_{\bar{\Lambda}}\overline{\text{H}}\right) = 238 \pm 33(\text{stat.}) \pm 28(\text{sys.})\ \text{ps},$$
$$\tau\left({}^4_\Lambda\text{H}\right) = 188 \pm 89(\text{stat.}) \pm 37(\text{sys.})\ \text{ps},$$
$$\tau\left({}^4_{\bar{\Lambda}}\overline{\text{H}}\right) = 170 \pm 72(\text{stat.}) \pm 34(\text{sys.})\ \text{ps}.$$

As shown in Fig. 4b, our results are consistent with most existing measurements within uncertainties[7,11,28,31–41], and theoretical predictions[42–47]. The lifetime differences between hypernuclei and their corresponding anti-hypernuclei are $\tau\left({}^3_\Lambda\text{H}\right) - \tau\left({}^3_{\bar{\Lambda}}\overline{\text{H}}\right) = 16 \pm 43(\text{stat.}) \pm 20(\text{sys.})$ ps and

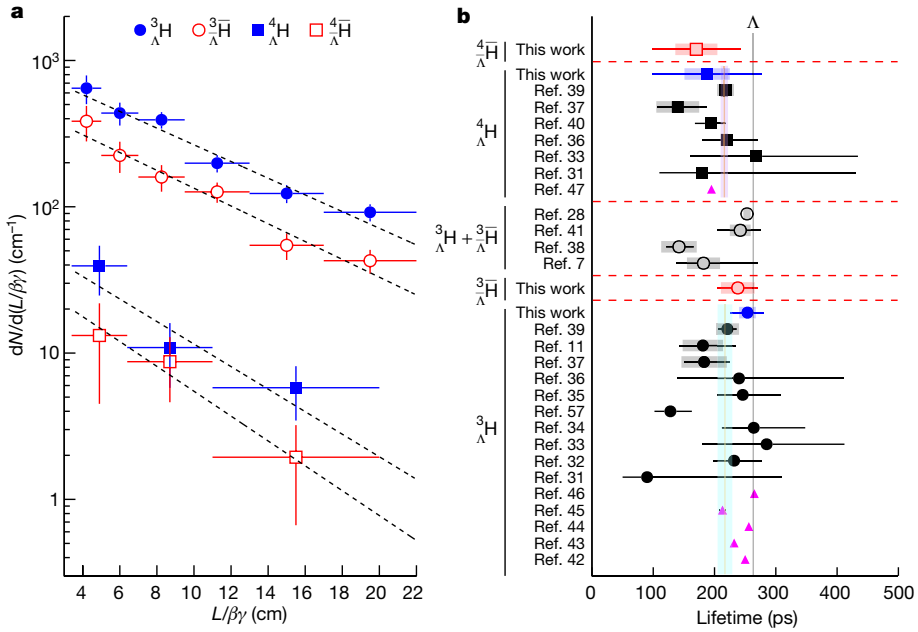

Fig. 4 | Hypernuclei dN/d($L/\beta\gamma$) as a function of $L/\beta\gamma$ and their lifetimes. **a**, ${}^{3}_{\Lambda}\mathrm{H}$, ${}^{3}_{\Lambda}\overline{\mathrm{H}}$, ${}^{4}_{\Lambda}\mathrm{H}$ and ${}^{4}_{\Lambda}\overline{\mathrm{H}}$ yields versus $L/\beta\gamma$. The vertical error bars represent the statistical uncertainties only. **b**, Our measured ${}^{3}_{\Lambda}\mathrm{H}$, ${}^{3}_{\Lambda}\overline{\mathrm{H}}$, ${}^{4}_{\Lambda}\mathrm{H}$ and ${}^{4}_{\Lambda}\overline{\mathrm{H}}$ lifetimes compared with world data[7,11,28,31–41,57] and theoretical predictions[42–47] (solid triangles). Error bars and boxes show statistical and systematic uncertainties, respectively. Solid vertical lines with shaded regions represent the average lifetimes of ${}^{3}_{\Lambda}\mathrm{H}$ and ${}^{4}_{\Lambda}\mathrm{H}$ and their corresponding uncertainties. These values are calculated from the previous results by a maximum-likelihood fit. The vertical grey line shows the lifetime of the free Λ.

$\tau\left({}^{4}_{\Lambda}\mathrm{H}\right) - \tau\left({}^{4}_{\Lambda}\overline{\mathrm{H}}\right) = 18 \pm 115(\mathrm{stat.}) \pm 46(\mathrm{sys.})$ ps. Both are consistent with zero within uncertainties, showing no difference between the properties of matter particles and those of their corresponding antimatter particles. This is a new test of the *CPT* symmetry.

Yield ratios

The (anti)nucleus and (anti)hypernucleus production yields carry information about their production mechanism in relativistic heavy-ion collisions. Collisions at RHIC energies create fireballs with a temperature of several hundred MeV (ref. 48), which corresponds to 10^{12} K, whereas the (anti)nuclei and (anti)hypernuclei have typical binding energies of merely several MeV per (anti)baryon. Thus, it is often imagined that these fragile objects are produced in the last stage of the collision-system evolution, by coalescence of (anti)hyperons and (anti)nucleons that are by chance close in both coordinate and momentum space[49–51]. As observed in earlier measurements[8,12], the probability to coalesce decreases by two to three orders of magnitude with each additional (anti)baryon. As the Λ baryon is heavier than the nucleons, it takes more energy to be created. There are fewer Λ baryons than protons and neutrons created in the fireballs. Thus, (anti)hypernucleus production yields are usually lower than those of (anti)nuclei with the same baryon numbers[7,11]. These baryon numbers and strangeness dependencies of particle production yields can also be well described by the statistical thermal model[48], which assumes all particles to be in thermal and chemical equilibrium. The parameters of the statistical thermal model (chemical freeze-out temperature T and baryon chemical potential μ_B) can be obtained by a simultaneous fit to all existing measured particle yields.

This analysis uses a combination of data from U + U, Au + Au, Ru + Ru and Zr + Zr collision systems, with different particle production yields. Thus, the absolute (anti)hypernuclear production yields in this mixture of collision systems are not well-defined physical quantities to measure. Instead, we measure various yield ratios among (anti)nuclei and (anti)hypernuclei with the same number of (anti)baryons. In this way, the yield differences due to different collision-system sizes will largely cancel out. The measurement is done with particles in a phase-space region of rapidity $|y| < 0.7$ (that is, the velocity component along the beam direction in the range of $|v_z| < 0.604c$) and $0.7 < p_T/m < 1.5$, where p_T is the momentum in the plane transverse to the beam direction. Detector acceptance, efficiency and decay branching fractions are corrected for. Owing to the lack of conclusive theoretical or experimental results, we assume 0.25 as the decay branching fraction of ${}^{3}_{\Lambda}\mathrm{H} \to {}^{3}\mathrm{He} + \pi^-$ and ${}^{3}_{\Lambda}\overline{\mathrm{H}} \to {}^{3}\overline{\mathrm{He}} + \pi^+$ (refs. 7,11,39,52) and 0.50 for ${}^{4}_{\Lambda}\mathrm{H} \to {}^{4}\mathrm{He} + \pi^-$ and ${}^{4}_{\Lambda}\overline{\mathrm{H}} \to {}^{4}\overline{\mathrm{He}} + \pi^+$ (refs. 39,52). ${}^{3}\mathrm{He}$, ${}^{3}\overline{\mathrm{He}}$, ${}^{4}\mathrm{He}$ and ${}^{4}\overline{\mathrm{He}}$ yields are corrected for contributions from ${}^{3}_{\Lambda}\mathrm{H}$, ${}^{3}_{\Lambda}\overline{\mathrm{H}}$, ${}^{4}_{\Lambda}\mathrm{H}$ and ${}^{4}_{\Lambda}\overline{\mathrm{H}}$ decays when calculating the ratios.

Figure 5 shows the measured particle production yield ratios and a comparison to previous experimental results[7,8,11,53], as well as the statistical thermal model predictions[48]. As the ${}^{3}_{\Lambda}\mathrm{H}/{}^{3}\mathrm{He}$ and ${}^{3}_{\Lambda}\overline{\mathrm{H}}/{}^{3}\overline{\mathrm{He}}$ ratios are expected to increase with the collision-system size[54,55], we have also measured them in large (U + U, Au + Au) and small (Zr + Zr, Ru + Ru) systems separately, to compare with existing the measurements. The measured particle ratios are consistent with previous measurements, and we note that the ${}^{3}_{\Lambda}\mathrm{H}/{}^{3}\mathrm{He}$ and ${}^{3}_{\Lambda}\overline{\mathrm{H}}/{}^{3}\overline{\mathrm{He}}$ ratios in U + U and Au + Au collisions are lower than previous STAR results[7] by 2.8σ and 1.9σ, respectively.

Various antimatter-over-matter particle yield ratios are measured to be below unity because the colliding heavy ions carry positive baryon numbers, and consequently the collision system has positive baryon chemical potential. We also observe that ${}^{4}\overline{\mathrm{He}}/{}^{4}\mathrm{He} \approx {}^{3}\overline{\mathrm{He}}/{}^{3}\mathrm{He} \times \bar{\mathrm{p}}/\mathrm{p}$, ${}^{4}_{\Lambda}\overline{\mathrm{H}}/{}^{4}_{\Lambda}\mathrm{H} \approx {}^{3}_{\Lambda}\overline{\mathrm{H}}/{}^{3}_{\Lambda}\mathrm{H} \times \bar{\mathrm{p}}/\mathrm{p}$, ${}^{4}_{\Lambda}\mathrm{H}/{}^{4}\mathrm{He} \approx 4 \times {}^{3}_{\Lambda}\mathrm{H}/{}^{3}\mathrm{He}$ and ${}^{4}_{\Lambda}\overline{\mathrm{H}}/{}^{4}\overline{\mathrm{He}} \approx 4 \times {}^{3}_{\Lambda}\overline{\mathrm{H}}/{}^{3}\overline{\mathrm{He}}$, as expected in the coalescence[49,50] picture of (anti)nucleus and (anti)hypernucleus production. Here the factors 4 are introduced because both spin-0 and spin-1 states of ${}^{4}_{\Lambda}\mathrm{H}$ have enough binding energy so that no energetically allowed strong decay channels exist for them. Therefore, the spin-1 state, with a spin degeneracy of 3, will decay electromagnetically to the spin-0 ground state. This enhances the total measured ${}^{4}_{\Lambda}\mathrm{H}$ and ${}^{4}_{\Lambda}\overline{\mathrm{H}}$ production yield by a factor of 4, compared with ${}^{4}\mathrm{He}$ and ${}^{4}\overline{\mathrm{He}}$, which have only a spin-0 state[39]. Considering this

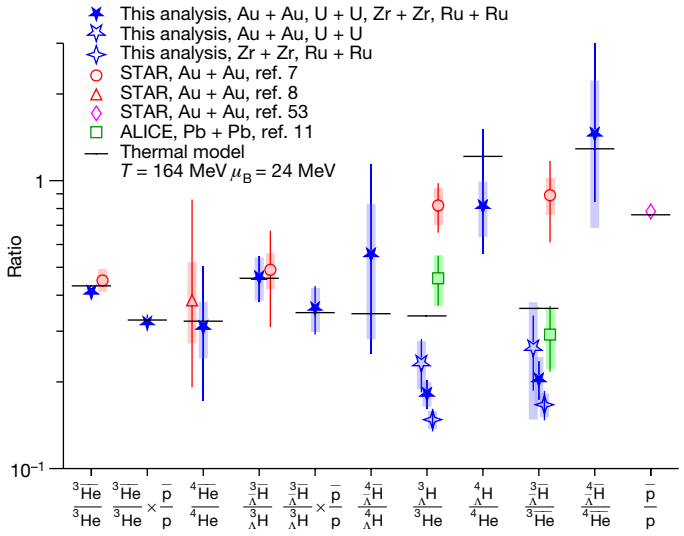

Fig. 5 | Production yield ratios among the various (anti)nuclei and (anti) hypernuclei with the same number of (anti)baryons. Results combining all collision systems in this work are shown by filled stars. Open stars show results with only U + U and Au + Au collisions, whereas quadrangular stars show results with only Zr + Zr and Ru + Ru collisions. Statistical uncertainties and systematic uncertainties are shown by vertical bars and shaded boxes, respectively. The decay branching fraction of ${}^{3}_{\Lambda}\mathrm{H} \to {}^{3}\mathrm{He} + \pi^{-}$ and ${}^{3}_{\Lambda}\overline{\mathrm{H}} \to {}^{3}\overline{\mathrm{He}} + \pi^{+}$ is assumed to be 0.25 (refs. 44,58), and the branching fraction of ${}^{4}_{\Lambda}\mathrm{H} \to {}^{4}\mathrm{He} + \pi^{-}$ and ${}^{4}_{\Lambda}\overline{\mathrm{H}} \to {}^{4}\overline{\mathrm{He}} + \pi^{+}$ is assumed to be 0.50 (refs. 59,60). Previous measurement results[7,8,11,53] and statistical-thermal-model predictions[48] are also shown for comparison.

spin-degeneracy effect, the statistical-thermal-model[48] predictions also match our measurements, except that the measured ${}^{3}_{\Lambda}\mathrm{H}/{}^{3}\mathrm{He}$ ratio is slightly lower than the statistical-thermal-model prediction. This difference, which is currently not statistically significant, may be explained by the very small binding energy of ${}^{3}_{\Lambda}\mathrm{H}$, which implies that the spatial extent of the ${}^{3}_{\Lambda}\mathrm{H}$ wave function is comparable to the whole collision system[54–56].

In general, our measured particle yield ratios are consistent with the expectation of the coalescence picture of (anti)nucleus and (anti) hypernucleus production and the statistical thermal model. Despite an enhancement factor of 4 because of the spin-degeneracy effect, the ${}^{4}_{\Lambda}\overline{\mathrm{H}}$ production yield is still about two orders of magnitude lower than that of ${}^{3}_{\Lambda}\overline{\mathrm{H}}$ (ref. 51). Fourteen years after the discovery of the first anti-hypernucleus ${}^{3}_{\Lambda}\overline{\mathrm{H}}$, 15.6 ${}^{4}_{\Lambda}\overline{\mathrm{H}}$ signal candidates are reconstructed and identified out of 6.4 billion collision events in this study, which is a substantial step forward in the experimental research of antimatter.

Online content

Any methods, additional references, Nature Portfolio reporting summaries, source data, extended data, supplementary information, acknowledgements, peer review information; details of author contributions and competing interests; and statements of data and code availability are available at https://doi.org/10.1038/s41586-024-07823-0.

1. STAR Collaboration et al. Experimental and theoretical challenges in the search for the quark–gluon plasma: the STAR Collaboration's critical assessment of the evidence from RHIC collisions. *Nucl. Phys. A* **757**, 102–183 (2005).
2. PHENIX Collaboration et al. Formation of dense partonic matter in relativistic nucleus–nucleus collisions at RHIC: experimental evaluation by the PHENIX Collaboration. *Nucl. Phys. A* **757**, 184–283 (2005).
3. PHOBOS Collaboration et al. The PHOBOS perspective on discoveries at RHIC. *Nucl. Phys. A* **757**, 28–101 (2005).
4. Arsene, I. et al. Quark–gluon plasma and color glass condensate at RHIC? The perspective from the BRAHMS experiment. *Nucl. Phys. A* **757**, 1–27 (2005).
5. Muller, B., Schukraft, J. & Wyslouch, B. First results from Pb+Pb collisions at the LHC. *Annu. Rev. Nucl. Part. Sci.* **62**, 361–386 (2012).
6. Adam, J. et al. Beam energy dependence of (anti-)deuteron production in Au+Au collisions at the BNL Relativistic Heavy Ion Collider. *Phys. Rev. C* **99**, 064905 (2019).
7. The STAR Collaboration et al. Observation of an antimatter hypernucleus. *Science* **328**, 58–62 (2010).
8. The STAR Collaboration et al. Observation of the antimatter helium-4 nucleus. *Nature* **473**, 353–356 (2011).
9. Chen, J., Keane, D., Ma, Y.-G., Tang, A. & Xu, Z. Antinuclei in heavy-ion collisions. *Phys. Rep.* **760**, 1–39 (2018).
10. The STAR Collaboration Measurement of the mass difference and the binding energy of the hypertriton and antihypertriton. *Nat. Phys.* **16**, 409–412 (2020).
11. ALICE Collaboration. ${}^{3}_{\Lambda}\mathrm{H}$ and ${}^{3}_{\Lambda}\overline{\mathrm{H}}$ production in Pb–Pb collisions at $\sqrt{s_{\mathrm{NN}}} = 2.76$ TeV. *Phys. Lett. B* **754**, 360–372 (2016).
12. ALICE Collaboration. Production of ${}^{4}\mathrm{He}$ and ${}^{4}\overline{\mathrm{He}}$ in Pb–Pb collisions at $\sqrt{s_{\mathrm{NN}}} = 2.76$ TeV at the LHC. *Nucl. Phys. A* **971**, 1–20 (2018).
13. ALICE Collaboration Precision measurement of the mass difference between light nuclei and anti-nuclei. *Nat. Phys.* **11**, 811–814 (2015).
14. Braun-Munzinger, P. & Dönigus, B. Loosely-bound objects produced in nuclear collisions at the LHC. *Nucl. Phys. A* **987**, 144–201 (2019).
15. Ackermann, K. H. et al. STAR detector overview. *Nucl. Instrum. Methods A* **499**, 624–632 (2003).
16. Harrison, M., Ludlam, T. & Ozaki, S. RHIC project overview. *Nucl. Instrum. Methods A* **499**, 235–244 (2003).
17. Dirac, P. A. M. The quantum theory of the electron. *Proc. R. Soc. Lond. A* **117**, 610–624 (1928).
18. Dirac, P. A. M. Quantised singularities in the electromagnetic field. *Proc. R. Soc. Lond. A* **133**, 60–72 (1931).
19. Anderson, C. D. The positive electron. *Phys. Rev.* **43**, 491–494 (1933).
20. Chamberlain, O., Segrè, E., Wiegand, C. & Ypsilantis, T. Observation of antiprotons. *Phys. Rev.* **100**, 947–950 (1955).
21. Cork, B., Lambertson, G. R., Piccioni, O. & Wenzel, W. A. Antineutrons produced from antiprotons in charge-exchange collisions. *Phys. Rev.* **104**, 1193–1197 (1956).
22. Prowse, D. J. & Baldo-Ceolin, M. Anti-lambda hyperon. *Phys. Rev. Lett.* **1**, 179–180 (1958).
23. Massam, T., Muller, Th., Righini, B., Schneegans, M. & Zichichi, A. Experimental observation of antideuteron production. *Nuovo Cim.* **39**, 10–14 (1965).
24. Dorfan, D. E., Eades, J., Lederman, L. M., Lee, W. & Ting, C. C. Observation of antideuterons. *Phys. Rev. Lett.* **14**, 1003–1006 (1965).
25. Antipov, Y. M. et al. Observation of anti-He-3. *Yad. Fiz.* **12**, 311–322 (1970).
26. Vishnevsky, N. K. et al. Observation of anti-tritium. *Yad. Fiz.* **20**, 694–708 (1974).
27. Aguilar, M. et al. Antiproton flux, antiproton-to-proton flux ratio, and properties of elementary particle fluxes in primary cosmic rays measured with the Alpha Magnetic Spectrometer on the International Space Station. *Phys. Rev. Lett.* **117**, 091103 (2016).
28. Acharya, S. et al. Measurement of the lifetime and Λ separation energy of ${}^{3}_{\Lambda}\mathrm{H}$. *Phys. Rev. Lett.* **131**, 102302 (2023).
29. Pérez-Obiol, A., Gazda, D., Friedman, E. & Gal, A. Revisiting the hypertriton lifetime puzzle. *Phys. Lett. B* **811**, 135916 (2020).
30. Gal, A., Hungerford, E. V. & Millener, D. J. Strangeness in nuclear physics. *Rev. Mod. Phys.* **88**, 035004 (2016).
31. Prem, R. J. et al. Lifetimes of hypernuclei ${}^{3}_{\Lambda}\mathrm{H}$, ${}^{4}_{\Lambda}\mathrm{H}$, ${}^{5}_{\Lambda}\mathrm{H}$. *Phys. Rev.* **136**, B1803 (1964).
32. Keyes, G. et al. New measurement of the ${}^{3}_{\Lambda}\mathrm{H}$. *Phys. Rev. Lett.* **20**, 819–821 (1968).
33. Phillips, R. E. et al. Lifetimes of light hyperfragments. II. *Phys. Rev.* **180**, 1307 (1969).
34. Keys, G. et al. Properties of ${}^{3}_{\Lambda}\mathrm{H}$. *Phys. Rev. D* **1**, 66–77 (1970).
35. Keys, G. et al. A measurement of the lifetime of the ${}^{5}_{\Lambda}\mathrm{H}$ hypernucleus. *Nucl. Phys. B* **67**, 269–283 (1973).
36. Avramenko, S. et al. A study of the production and lifetime of the lightest relativistic hypernuclei. *Nucl. Phys. A* **547**, 95–100 (1992).
37. Rappold, C. et al. Hypernuclear spectroscopy of products from ${}^{6}\mathrm{Li}$ projectiles on a carbon target at 2 A GeV. *Nucl. Phys. A* **913**, 170–184 (2013).
38. Adamczyk, L. et al. Measurement of the ${}^{3}_{\Lambda}\mathrm{H}$ lifetime in Au+Au collisions at the BNL relativistic heavy ion collider. *Phys. Rev. C* **97**, 054909 (2018).
39. Abdallah, M. et al. Measurements of ${}^{3}_{\Lambda}\mathrm{H}$ and ${}^{4}_{\Lambda}\mathrm{H}$ lifetimes and yields in Au+Au collisions in the high baryon density region. *Phys. Rev. Lett.* **128**, 202301 (2022).
40. Outa, H. et al. Mesonic weak decay of ${}^{4}_{\Lambda}\mathrm{H}$ and ${}^{4}_{\Lambda}\mathrm{He}$. *Nucl. Phys. A* **585**, 109–112 (1995).
41. Acharya, S. et al. ${}^{3}_{\Lambda}\mathrm{H}$ and ${}^{3}_{\Lambda}\overline{\mathrm{H}}$ lifetime measurement in Pb-Pb collisions at $\sqrt{s_{\mathrm{NN}}}$ 5.02 TeV via two-body decay. *Phys. Lett. B* **797**, 134905 (2019).
42. Rayet, M. & Dalitz, R. H. The lifetime of ${}^{3}_{\Lambda}\mathrm{H}$. *Nuovo Cim.* **XLVI**, 8302–8310 (1966).
43. Congleton, J. G. A simple model of the hypertriton. *J. Phys. G Nucl. Part. Phys.* **18**, 339–357 (1992).
44. Kamada, H. et al. π-Mesonic decay of the hypertriton. *Phys. Rev. C* **57**, 1595–1603 (1998).
45. Gal, A. et al. Towards resolving the ${}^{3}_{\Lambda}\mathrm{H}$ lifetime puzzle. *Phys. Lett. B* **791**, 48–53 (2019).
46. Hildenbrand, F. & Hammer, H.-W. Lifetime of the hypertriton. *Phys. Rev. C* **102**, 064002 (2020).
47. Gal, A. Recent progress on few-body hypernuclei. *EPJ Web Conf.* **259**, 08002 (2022).
48. Andronic, A., Braun-Munzinger, P., Stachel, J. & Stöcker, H. Production of light nuclei, hypernuclei and their antiparticles in relativistic nuclear collisions. *Phys. Lett. B* **697**, 203–207 (2011).
49. Sato, H. & Yazaki, K. On the coalescence model for high energy nuclear reactions. *Phys. Lett. B* **98**, 153–157 (1981).
50. Steinheimer, J. et al. Hypernuclei, dibaryon and antinuclei production in high energy heavy ion collisions: thermal production vs. coalescence. *Phys. Lett. B* **714**, 85–91 (2012).
51. Sun, K.-J. & Chen, L.-W. Antimatter ${}^{4}_{\Lambda}\mathrm{H}$ hypernucleus production and the ${}^{3}_{\Lambda}\mathrm{H}/{}^{3}\mathrm{He}$ puzzle in relativistic heavy-ion collisions. *Phys. Rev. C* **93**, 064909 (2016).
52. Armstrong, T. A. et al. Production of ${}^{3}_{\Lambda}\mathrm{H}$ and ${}^{4}_{\Lambda}\mathrm{H}$ in central 11.5-GeV/c Au+Pt heavy ion collisions. *Phys. Rev. C* **70**, 024902 (2004).
53. Abelev, B. I. et al. Identified baryon and meson distributions at large transverse momenta from Au+Au collisions at $\sqrt{s_{\mathrm{NN}}} = 200$ GeV. *Phys. Rev. Lett.* **97**, 152301 (2006).

54. Sun, K.-J., Ko, C. M. & Dönigus, B. Suppression of light nuclei production in collisions of small systems at the Large Hadron Collider. *Phys. Lett. B* **792**, 132–137 (2019).
55. Bellini, F. & Kalweit, A. P. Testing production scenarios for (anti-)(hyper-)nuclei and exotica at energies available at the CERN Large Hadron Collider. *Phys. Rev. C* **99**, 054905 (2019).
56. Armstrong, T. A. et al. Mass dependence of light-nucleus production in ultrarelativistic heavy-ion collisions. *Phys. Rev. Lett.* **83**, 5431–5434 (1999).
57. Bohm, G. et al. On the lifetime of the $^{3}_{\Lambda}$H hypernucleus. *Nucl. Phys. B* **16**, 46–52 (1970).
58. Glöckle, W., Miyagawa, K., Kamada, H., Golak, J. & Witala, H. The hypertriton and its decays. *Nucl. Phys. A* **639**, 297c–306c (1998).
59. Kumagai-Fuse, I., Okabe, S. & Akaishi, Y. Pauli effects on pionic decay of light Lambda hypernuclei. *Nucl. Phys. A* **585**, 365c–366c (1995).
60. Outa, H. et al. Mesonic and non-mesonic decay widths of $^{4}_{\Lambda}$H and $^{4}_{\Lambda}$He. *Nucl. Phys. A* **639**, 251c–260c (1998).

STAR Collaboration

M. I. Abdulhamid[1], B. E. Aboona[2], J. Adam[3], L. Adamczyk[4], J. R. Adams[5], I. Aggarwal[6], M. M. Aggarwal[6], Z. Ahammed[7], E. C. Aschenauer[8], S. Aslam[9], J. Atchison[10], V. Bairathi[11], J. G. Ball Cap[12], K. Barish[13], R. Bellwied[12], P. Bhagat[14], A. Bhasin[14], S. Bhatta[15], S. R. Bhosale[16], J. Bielcik[3], J. Bielcikova[17], J. D. Brandenburg[5], C. Broodo[12], X. Z. Cai[18], H. Caines[19], M. Calderón de la Barca Sánchez[20], D. Cebra[20], J. Ceska[3], I. Chakaberia[21], P. Chaloupka[3], B. K. Chan[22], Z. Chang[23], A. Chatterjee[24], D. Chen[13], J. Chen[25], J. H. Chen[26], Z. Chen[25], J. Cheng[27], Y. Cheng[22], S. Choudhury[26], W. Christie[8], X. Chu[8], H. J. Crawford[28], M. Csanád[16], G. Dale-Gau[29], A. Das[3], I. M. Deppner[30], A. Dhamija[6], P. Dixit[31], X. Dong[21], J. L. Drachenberg[10], E. Duckworth[32], J. C. Dunlop[8], J. Engelage[28], G. Eppley[33], S. Esumi[34], O. Evdokimov[29], O. Eyser[8], R. Fatemi[35], S. Fazio[36], C. J. Feng[37], Y. Feng[38], E. Finch[39], Y. Fisyak[8], F. A. Flor[19], C. Fu[40], C. A. Gagliardi[2], T. Galatyuk[41], T. Gao[25], F. Geurts[33], N. Ghimire[42], A. Gibson[43], K. Gopal[44], X. Gou[25], D. Grosnick[43], A. Gupta[14], W. Guryn[8], A. Hamed[1], Y. Han[33], S. Harabasz[41], M. D. Harasty[20], J. W. Harris[19], H. Harrison-Smith[35], W. He[26], X. H. He[40], Y. He[25], N. Herrmann[30], L. Holub[3], C. Hu[45], Q. Hu[40], Y. Hu[21], H. Huang[37], H. Z. Huang[22], S. L. Huang[15], T. Huang[29], X. Huang[27], Y. Huang[27], Y. Huang[46], T. J. Humanic[5], M. Isshiki[34], W. W. Jacobs[23], A. Jalotra[14], C. Jena[44], A. Jentsch[8], Y. Ji[21], J. Jia[8,15], C. Jin[33], X. Ju[47], E. G. Judd[28], S. Kabana[11], D. Kalinkin[35], K. Kang[27], D. Kapukchyan[13], K. Kauder[8], D. Keane[32], A. Khanal[48], Y. V. Khyzhniak[5], D. P. Kikoła[49], D. Kincses[16], I. Kisel[50], A. Kiselev[8], A. G. Knospe[51], H. S. Ko[21], L. K. Kosarzewski[5], L. Kumar[6], M. C. Labonte[20], R. Lacey[15], J. M. Landgraf[8], J. Lauret[8], A. Lebedev[8], J. H. Lee[8], Y. H. Leung[30], N. Lewis[8], C. Li[46], D. Li[47], H-S. Li[38], H. Li[52], W. Li[33], X. Li[47], Y. Li[47], Y. Li[27], Z. Li[47], X. Liang[13], Y. Liang[32], R. Licenik[3,17], T. Lin[25], Y. Lin[53], M. A. Lisa[5], C. Liu[40], G. Liu[54], H. Liu[46], L. Liu[46], T. Liu[19], X. Liu[5], Y. Liu[2], Z. Liu[46], T. Ljubicic[33], O. Lomicky[3], R. S. Longacre[8], E. M. Loyd[13], T. Lu[40], J. Luo[47], X. F. Luo[46], L. Ma[26], R. Ma[8], Y. G. Ma[26], N. Magdy[15], D. Mallick[49], R. Manikandhan[12], S. Margetis[32], C. Markert[55], G. McNamara[48], O. Mezhanska[3], K. Mi[46], S. Mioduszewski[2], B. Mohanty[56], M. M. Mondal[56], I. Mooney[19], J. Mrazkova[3,17], M. I. Nagy[16], A. S. Nain[6], J. D. Nam[42], M. Nasim[31], D. Neff[22], J. M. Nelson[28], D. B. Nemes[19], M. Nie[25], G. Nigmatkulov[29], T. Niida[34], T. Nonaka[34], G. Odyniec[21], A. Ogawa[8], S. Oh[57], K. Okubo[34], B. S. Page[8], R. Pak[8], S. Pal[3], A. Pandav[21], A. K. Pandey[40], T. Pani[58], A. Paul[13], B. Pawlik[59], D. Pawlowska[49], C. Perkins[28], J. Pluta[49], B. R. Pokhrel[42], M. Posik[42], T. Protzman[51], V. Prozorova[3], N. K. Pruthi[6], M. Przybycien[4], J. Putschke[48], Z. Qin[27], H. Qiu[40], C. Racz[13], S. K. Radhakrishnan[32], A. Rana[6], R. L. Ray[55], R. Reed[51], C. W. Robertson[38], M. Robotkova[3,17], M. A. Rosales Aguilar[35], D. Roy[58], P. Roy Chowdhury[49], L. Ruan[8], A. K. Sahoo[31], N. R. Sahoo[44], H. Sako[34], S. Salur[58], S. Sato[34], B. C. Schaefer[51], W. B. Schmidke[8,68], N. Schmitz[60], F-J. Seck[41], J. Seger[61], R. Seto[13], P. Seyboth[60], N. Shah[9], P. V. Shanmuganathan[8], T. Shao[26], M. Sharma[14], N. Sharma[31], R. Sharma[44], S. R. Sharma[44], A. I. Sheikh[32], D. Shen[25], D. Y. Shen[26], K. Shen[47], S. S. Shi[46], Y. Shi[25], Q. Y. Shou[26], F. Si[47], J. Singh[6], S. Singha[40], P. Sinha[44], M. J. Skoby[38,62], N. Smirnov[19], Y. Söhngen[30], Y. Song[19], B. Srivastava[38], T. D. S. Stanislaus[43], M. Stefaniak[5], D. J. Stewart[48], Y. Su[47], M. Sumbera[17], C. Sun[15], X. Sun[40], Y. Sun[47], Y. Sun[63], B. Surrow[42], M. Svoboda[3,17], Z. W. Sweger[20], A. C. Tamis[19], A. H. Tang[8], Z. Tang[47], T. Tarnowsky[64], J. H. Thomas[21], A. R. Timmins[12], D. Tlusty[61], T. Todoroki[34], S. Trentalange[22], P. Tribedy[8], S. K. Tripathy[49], T. Truhlar[3], B. A. Trzeciak[3], O. D. Tsai[8,22], C. Y. Tsang[8,32], Z. Tu[8], J. Tyler[2], T. Ullrich[8], D. G. Underwood[43,65], I. Upsal[47], G. Van Buren[8], J. Vanek[8], I. Vassiliev[50], V. Verkest[48], F. Videbæk[8], S. A. Voloshin[48], F. Wang[38], G. Wang[22], J. S. Wang[63], J. Wang[25], K. Wang[47], X. Wang[25], Y. Wang[47], Y. Wang[46], Y. Wang[27], Z. Wang[25], J. C. Webb[8], P. C. Weidenkaff[30], G. D. Westfall[64], D. Wielanek[49], H. Wieman[21], G. Wilks[29], S. W. Wissink[23], R. Witt[66], J. Wu[46], J. Wu[40], X. Wu[22], X. Wu[47], B. Xi[26], Z. G. Xiao[27], G. Xie[45], W. Xie[38], H. Xu[63], N. Xu[21], Q. H. Xu[25], Y. Xu[25], Y. Xu[46], Z. Xu[32], Z. Xu[22], G. Yan[25], Z. Yan[15], C. Yang[25], Q. Yang[25], S. Yang[54], Y. Yang[37], Z. Ye[54], Z. Ye[21], L. Yi[25], K. Yip[8], Y. Yu[25], H. Zbroszczyk[49], W. Zha[47], C. Zhang[26], D. Zhang[54], J. Zhang[25], S. Zhang[67], W. Zhang[54], X. Zhang[40], Y. Zhang[40], Y. Zhang[47], Y. Zhang[25], Y. Zhang[46], Z. J. Zhang[37], Z. Zhang[8], Z. Zhang[29], F. Zhao[40], J. Zhao[26], M. Zhao[8], J. Zhou[47], S. Zhou[46], Y. Zhou[46], X. Zhu[27], M. Zurek[8,65] & M. Zyzak[50]

[1]American University in Cairo, New Cairo, Egypt. [2]Texas A&M University, College Station, TX, USA. [3]Faculty of Nuclear Sciences and Physical Engineering, Czech Technical University in Prague, Prague, Czech Republic. [4]Faculty of Physics and Applied Computer Science, AGH University of Krakow, Cracow, Poland. [5]The Ohio State University, Columbus, OH, USA. [6]Panjab University, Chandigarh, India. [7]Variable Energy Cyclotron Centre, Kolkata, India. [8]Brookhaven National Laboratory, Upton, NY, USA. [9]Indian Institute Technology, Patna, India. [10]Abilene Christian University, Abilene, TX, USA. [11]Instituto de Alta Investigación, Universidad de Tarapacá, Arica, Chile. [12]University of Houston, Houston, TX, USA. [13]University of California, Riverside, Riverside, TX, USA. [14]University of Jammu, Jammu, India. [15]State University of New York, Stony Brook, NY, USA. [16]ELTE Eötvös Loránd University, Budapest, Hungary. [17]Nuclear Physics Institute of the CAS, Rez, Czech Republic. [18]Shanghai Institute of Applied Physics, Chinese Academy of Sciences, Shanghai, China. [19]Yale University, New Haven, CT, USA. [20]University of California, Davis, Davis, CA, USA. [21]Lawrence Berkeley National Laboratory, Berkeley, CA, USA. [22]University of California, Los Angeles, Los Angeles, CA, USA. [23]Indiana University, Bloomington, IN, USA. [24]National Institute of Technology, Durgapur, India. [25]Shandong University, Qingdao, China. [26]Fudan University, Shanghai, China. [27]Tsinghua University, Beijing, China. [28]University of California, Berkeley, Berkeley, CA, USA. [29]University of Illinois at Chicago, Chicago, IL, USA. [30]University of Heidelberg, Heidelberg, Germany. [31]Indian Institute of Science Education and Research, Berhampur, India. [32]Kent State University, Kent, OH, USA. [33]Rice University, Houston, TX, USA. [34]University of Tsukuba, Tsukuba, Ibaraki, Japan. [35]University of Kentucky, Lexington, KY, USA. [36]University of Calabria and INFN-Cosenza, Rende, Italy. [37]National Cheng Kung University, Tainan, Taiwan. [38]Purdue University, West Lafayette, IN, USA. [39]Southern Connecticut State University, New Haven, CT, USA. [40]Institute of Modern Physics, Chinese Academy of Sciences, Lanzhou, China. [41]Technische Universität Darmstadt, Darmstadt, Germany. [42]Temple University, Philadelphia, PA, USA. [43]Valparaiso University, Valparaiso, IN, USA. [44]Indian Institute of Science Education and Research, Tirupati, India. [45]University of Chinese Academy of Sciences, Beijing, China. [46]Central China Normal University, Wuhan, China. [47]University of Science and Technology of China, Hefei, China. [48]Wayne State University, Detroit, MI, USA. [49]Warsaw University of Technology, Warsaw, Poland. [50]Frankfurt Institute for Advanced Studies, Frankfurt, Germany. [51]Lehigh University, Bethlehem, PA, USA. [52]Wuhan University of Science and Technology, Wuhan, China. [53]Guangxi Normal University, Guilin, China. [54]South China Normal University, Guangzhou, China. [55]University of Texas, Austin, TX, USA. [56]National Institute of Science Education and Research, Homi Bhabha National Institute, Jatni, India. [57]Sejong University, Seoul, South Korea. [58]Rutgers University, Piscataway, NJ, USA. [59]Institute of Nuclear Physics PAN, Cracow, Poland. [60]Max-Planck-Institut für Physik, Munich, Germany. [61]Creighton University, Omaha, NE, USA. [62]Ball State University, Muncie, IN, USA. [63]Huzhou University, Huzhou, China. [64]Michigan State University, East Lansing, MI, USA. [65]Argonne National Laboratory, Argonne, IL, USA. [66]United States Naval Academy, Annapolis, MD, USA. [67]Chongqing University, Chongqing, China. [68]Deceased: W. B. Schmidke.

Methods

Event sample and trigger selection

This analysis used 606 million and 624 million $\sqrt{s_{NN}}$ = 200 GeV Au + Au collision events obtained in the years 2010 and 2011, 512 million $\sqrt{s_{NN}}$ = 193 GeV U + U collision events from the year 2012 and 4.7 billion $\sqrt{s_{NN}}$ = 200 GeV Ru + Ru and Zr + Zr collision events from the year 2018.

Most of the events were collected with minimum-bias triggers. The minimum-bias triggers are designed to accept the events with different impact parameters as equally as possible. The minimum-bias triggers required a coincidence between either the vertex-position detectors (VPD) or the zero-degree calorimeters (ZDC). The VPD (ref. 61) is a pair of timing detectors mounted directly around the beampipe that covers approximately half of the phase space over the pseudorapidity region $4.2 < |\eta| < 5.2$. The ZDC (ref. 62) is a pair of hadronic calorimeters located at $|\eta| > 6.6$ that detect spectator neutrons emerging from heavy-ion collisions.

Often the minimum-bias triggers were highly prescaled to reserve a fraction of the data-acquisition bandwidth for triggers on rare processes. Events that satisfied central or non-photonic electron triggers were included in the analysis to enhance the overall statistics. The central triggers combined multiplicity information from the TOF system[63] with spectator-neutron multiplicity information from the ZDCs to select collisions with small impact parameters. The non-photonic electron triggers, intended primarily to select events containing electrons from charm- and bottom-quark decays, required a large transverse energy deposition ($E_T > 2.6$ GeV, 3.5 GeV or 4.2 GeV) in at least one $\Delta\eta \times \Delta\phi = 0.05 \times 0.05$ tower in the barrel electromagnetic calorimeter[64]. They have a high probability of triggering on events containing antinuclei, which may annihilate in the electromagnetic calorimeter. Events triggered by the central or non-photonic electron triggers were not used in the yield ratios analysis to avoid potential biases.

The reconstructed collision point, called the primary vertex, is required to be within 2 cm of the beamline and within 40 cm along the beam line from the detector centre.

Daughter-particle identification

Information from the TPC[65] and the TOF[63] are combined for particle identification. The cylindrical TPC has full azimuthal coverage in the pseudorapidity range of $-1 < \eta < 1$. To ensure good track quality, a minimum of 20 measured points in TPC is required for all tracks used in this analysis. The average particle energy loss $\langle dE/dx \rangle$ versus rigidity is theoretically described with the Bichsel function[66]. A selected ^{3}He or $^3\overline{\text{He}}$ candidate should satisfy $|n_{\sigma^3\text{He}}| < 3$. If the track has matched TOF hit information, it should also satisfy the condition $1.0 < m^2/Z^2 < 3.0$ (GeV c^{-2})^2. For ^{4}He and $^4\overline{\text{He}}$ selection, apart from $|n_{\sigma^4\text{He}}| < 3$, it is also required that $2.8 < m^2/Z^2 < 4.1$ (GeV c^{-2})^2, if a matching TOF hit is present, or $|n_{\sigma^3\text{He}}| > 3.5$, if there is no TOF match, to minimize contamination from ^{3}He and $^3\overline{\text{He}}$, which has much higher production yields. To reject background ^{3}He and ^{4}He knocked out from the beam pipe and other materials, the distance-of-closest approach (DCA) between the ^{3}He or ^{4}He trajectory and the primary vertex is required to be within 1 cm. This DCA requirement is not applied to $^3\overline{\text{He}}$ and $^4\overline{\text{He}}$ because there are no knock-out antinuclei. The daughter $\pi^\pm$ from (anti)hypernucleus decay is identified by requiring $|n_{\sigma\pi^\pm}| < 3$. An m^2/Z^2 cut is also applied if the track is associated with a TOF hit.

Topological reconstruction

(Anti)hypernucleus candidates are reconstructed from the selected $\pi^\pm$ and (anti)helium nucleus tracks by the Kalman Filter Particle Finder package[67–70], which is based on the Kalman filter method. The decay topology of a hypernucleus, as shown in Extended Data Fig. 1, is characterized by several variables: χ^2_{topo} describing the deviation of the reconstructed path of the mother particle from the primary vertex, χ^2_{NDF} describing the deviation between the two daughter tracks at the decay vertex, χ^2_{primary} describing the deviation of the decay daughter track from the primary vertex, the decay length (L) and L over its uncertainty (L/dL). The selection cuts on these topological variables are optimized for the best $^3_\Lambda\overline{\text{H}}$ signal, instead of the $^4_\Lambda\overline{\text{H}}$ signal, to avoid any bias towards a better signal and a larger yield of $^4_\Lambda\overline{\text{H}}$ because of statistical fluctuations. This bias due to fluctuations is much smaller for $^3_\Lambda\overline{\text{H}}$ because of its large signal significance. The optimized topological-selection cuts are listed in Extended Data Table 1. Most selections are applied such that the two daughter tracks are likely to come from a common decay vertex with significant displacement from the collision point. As the (anti)helium is much heavier than the decay daughter pion, the momentum and track direction of the (anti)helium are very close to those of the parent (anti)hypernuclei. Thus, the (anti)helium DCA due to decay is too small to be observed with STAR-TPC tracking resolution, and a lower limit on He χ^2_{primary} does not help to improve the signal. The very loose upper limit on He χ^2_{primary} is used here to reject background helium candidate tracks that are too far away from the collision point, for example, from pile-up events.

The invariant mass of a (anti)hypernucleus candidate is calculated as $\sqrt{(E_{\text{He}} + E_\pi)^2 - (\mathbf{p}_{\text{He}} + \mathbf{p}_\pi)^2}$, where E and $\mathbf{p}$ are the energy and three-dimensional momentum of the daughter particles.

Background subtraction

The invariant-mass distributions of the combinatorial backgrounds are reproduced with the rotation method. Before a helium track is paired with a pion track, its azimuthal angle ϕ is rotated randomly in a range of [30°, 330°]. This procedure is repeated 50 times to increase the statistics. Then the same topological-selection cuts as for signal-candidate selection are applied for the rotational background. These cuts are then scaled so that their integrals in two side-band regions (2.941 - 2.987 GeV c^{-2} and 2.997 - 3.101 GeV c^{-2} for $^3_\Lambda$H and $^3_\Lambda\overline{\text{H}}$, and 3.859 - 3.919 GeV c^{-2} and 3.925 - 4.019 GeV c^{-2} for $^4_\Lambda$H and $^4_\Lambda\overline{\text{H}}$) are equal to the integrals of the signal-candidate invariant-mass distributions in the same regions. The statistical uncertainties in the rotational background are obtained with a bootstrapping method. After that, the signal counts are extracted by subtracting the integrals of the scaled combinatorial background distributions from the integrals of the signal-candidate distributions in the signal invariant-mass regions (2.987 - 2.997 GeV c^{-2} for $^3_\Lambda$H and $^3_\Lambda\overline{\text{H}}$, and 3.919 - 3.925 GeV c^{-2} for $^4_\Lambda$H and $^4_\Lambda\overline{\text{H}}$) (ref. 71).

Significance calculation

The signal significances in this analysis are obtained by calculating the likelihood ratios between the hypothesis of pure background and that of signal plus background. This is conducted both by counting the signal and background in a predefined signal invariant-mass region and by fitting the candidate invariant-mass distribution without and with the signal. In the counting method, the significance is calculated by the asymptotic formula[72]

$$Z_{\text{count}} = \sqrt{2\left[(N_{\text{Sig}} + N_{\text{Bg}})\ln\left(1 + \frac{N_{\text{Sig}}}{N_{\text{Bg}}}\right) - N_{\text{Sig}}\right]}, \quad (3)$$

where the signal count N_{Sig} and background count N_{Bg} are obtained as described in the previous paragraph. In the fitting method, the candidate invariant-mass distribution is first fit by pure rotational background with a free scaling factor, then fit by rotational background plus a Gaussian-shaped signal. The Gaussian shape is because of the measured daughter-particle momentum resolution, which is propagated to the calculated invariant mass. All the Gaussian parameters are free in the fit. The likelihood ratios between the fits without and with the Gaussian-shaped signals are used to calculate the significances Z_{shape}.

Efficiency correction

A correction is applied for the detector acceptance and reconstruction efficiency in the lifetime and yield-ratio measurements. The acceptance and efficiency are obtained with an embedding Monte Carlo technique. (Anti)hypernucleus decay and the paths of their daughters are simulated using the GEANT3 package[73], taking into account the geometry and materials of the STAR detectors[74]. The responses of the detectors and read-out electronics are also simulated, and the final simulated data are embedded into real-data events, which are sampled from different data-taking runs to have a good representation of the whole data set used in the analysis. The number of Monte Carlo (anti)hypernuclei embedded is 5% of the multiplicity of the real-data events. Then the embedded events are processed through the same reconstruction procedures as real data. After that, the same track and topological requirements as for the real data are applied to the reconstructed Monte Carlo (anti)hypernuclei. The final reconstruction efficiency ϵ is calculated as the ratio of the number of reconstructed Monte Carlo (anti) hypernuclei to the number of input Monte Carlo (anti)hypernuclei. This efficiency ϵ includes particle interaction with materials, detector acceptance, tracking efficiency and selection efficiency. As GEANT3 does not properly consider (anti)nucleus absorption by materials, we simulate the ^{3}He, $^3\overline{\text{He}}$, ^{4}He and $^4\overline{\text{He}}$ absorption using GEANT4, and further correct their track efficiency from the official STAR simulation. This correction is less than 3% for nuclei and less than 5% for antinuclei. The fraction of (anti)hypernuclei absorbed by the beam pipe (Be) and insulation gas (N_2) are estimated to be minimal and can be neglected.

The (anti)hypernucleus reconstruction efficiencies as a function of $L/(\beta\gamma)$ are shown in Extended Data Fig. 2, which are used to correct the raw yields in different $L/(\beta\gamma)$ intervals before the exponential fits are conducted to extract the lifetimes.

(Anti)hypernuclei, Λ and $\overline{\Lambda}$ lifetime measurements

Extended Data Fig. 3 shows the invariant-mass distributions of $^3_\Lambda$H, $^3_{\overline{\Lambda}}\overline{\text{H}}$, $^4_\Lambda$H and $^4_{\overline{\Lambda}}\overline{\text{H}}$ candidates in different $L/(\beta\gamma)$ intervals, which are used to extract their lifetimes. To avoid the low transverse momentum region, in which the reconstruction efficiency approaches zero and may have relatively large systematic uncertainties, the measurement is performed only for (anti)hypernuclei with $p_T > 2.1$ GeV c^{-1}.

As an additional test of (anti)hypernucleus lifetime measurements, we have also measured the Λ and $\overline{\Lambda}$ lifetimes with the same method. About 3.2 million Au + Au collision events at $\sqrt{s_{\text{NN}}} = 200$ GeV are used for these measurements. The topological cuts used to obtain the Λ signal are the same as those used in the (anti)hypernucleus analysis, except that an additional $\text{DCA}_{V_0} < 0.1$ cm topological cut is added. DCA_{V_0} is the distance-of-closest approach between the reconstructed mother-particle trajectory and the primary vertex. The DCA_{V_0} cut suppresses the contributions of Λ from Ξ and Ω decays and $\overline{\Lambda}$ from $\overline{\Xi}$ and $\overline{\Omega}$ decays, which make the measured lifetime longer. This is verified by the fact that the measured Λ and $\overline{\Lambda}$ lifetimes increase as the allowed DCA_{V_0} range is increased. Extended Data Fig. 4 shows the Λ and $\overline{\Lambda}$ $L/\beta\gamma$ distributions and the exponential fit to obtain their lifetimes. Our measured lifetimes for Λ (264.5 ± 1.6 ps) and $\overline{\Lambda}$ (268.3 ± 2.3 ps) are consistent considering uncertainties, as expected by the *CPT* symmetry. However, they are slightly longer than the value from the Particle Data Group 263 ± 2 ps (ref. 75). This is expected because the DCA_{V_0} cut cannot exclude all Λ from Ξ and Ω decays. No particle yet discovered decays weakly to $^3_\Lambda$H or $^4_\Lambda$H, so we do not consider the decay feed-down effect for (anti)hypernuclei lifetime measurements in this analysis.

Yield measurements

The yields of all the studied particles in this work are measured in the phase space of $|y| < 0.7$ and $0.7 < p_T/m < 1.5$ with only minimum-bias triggered events to avoid possible bias from the trigger selection. Thus, the (anti)hypernucleus signal counts are less than those in Fig. 3 in this paper. The signal and background counts that are used to extract (anti) hypernuclei yield ratios are listed in Extended Data Table 2.

After $|n_{\sigma^3\text{He}}| < 3$ and $1 < m^2/Z^2 < 3$ (GeV c^{-2})^2 selections, the ^{3}He and $^3\overline{\text{He}}$ candidates are counted with a $1/\epsilon$ weight to get the yield in the measured phase space.

For $^3_\Lambda$H and $^3_{\overline{\Lambda}}\overline{\text{H}}$ yield measurements, invariant-mass distributions are obtained with a candidate-by-candidate $1/\epsilon$ weight. Then the signal yield is extracted by subtracting the combinatorial background, obtained by the rotation method, from the candidate invariant-mass distribution in the signal range.

For ^{4}He, $^4\overline{\text{He}}$, $^4_\Lambda$H and $^4_{\overline{\Lambda}}\overline{\text{H}}$, the statistics are too low to apply a candidate-by-candidate efficiency correction. We thus calculated the total raw yields in the whole selected p_T range and corrected it by the average efficiency. The average efficiency is obtained based on knowledge of the p_T spectra of $A = 3$ (anti)(hyper)nuclei. First, the p_T spectra for ^{3}He, $^3\overline{\text{He}}$, $^3_\Lambda$H and $^3_{\overline{\Lambda}}\overline{\text{H}}$ are obtained and fitted with blast-wave functions[76]

$$\frac{1}{2\pi p_T}\frac{\mathrm{d}^2N}{\mathrm{d}p_T\mathrm{d}y} \propto \int_0^R r\,\mathrm{d}r m_0 I_0\left(\frac{p_T\sinh\rho}{T}\right)K_1\left(\frac{m_T\cosh\rho}{T}\right), \qquad (4)$$

as shown in Extended Data Fig. 5. Here $\rho = \tanh^{-1}(\beta_s(r/R)^n)$ and $n = 1$. The fireball radius R is fixed to 10 fm. I_0 and K_1 are Bessel functions, m_0 is the particle mass and $m_T = \sqrt{m_0^2 + p_T^2}$. β_s and T are free-fitting parameters, representing the expansion velocity and temperature of the fireball. We then assume the blast-wave functions for ^{4}He, $^4\overline{\text{He}}$, $^4_\Lambda$H and $^4_{\overline{\Lambda}}\overline{\text{H}}$ have the same β_s and T as for ^{3}He, $^3\overline{\text{He}}$, $^3_\Lambda$H and $^3_{\overline{\Lambda}}\overline{\text{H}}$, respectively, and the only difference in the blast-wave functions is the particle masses[71]. The efficiencies for ^{4}He, $^4\overline{\text{He}}$, $^4_\Lambda$H and $^4_{\overline{\Lambda}}\overline{\text{H}}$ in the whole measured p_T range are calculated as the average efficiency with the above blast-wave-function weights. The measured raw yields of ^{4}He, $^4\overline{\text{He}}$, $^4_\Lambda$H and $^4_{\overline{\Lambda}}\overline{\text{H}}$ are then corrected with the average efficiencies to obtain the reported yields.

The yields of ^{3}He, $^3\overline{\text{He}}$, ^{4}He and $^4\overline{\text{He}}$ are also corrected for the contributions from the weak decays of $^3_\Lambda$H, $^3_{\overline{\Lambda}}\overline{\text{H}}$, $^4_\Lambda$H and $^4_{\overline{\Lambda}}\overline{\text{H}}$, whose fractions out of the total measured (anti)helium nuclei yields are listed in Extended Data Table 3.

Although the measured particle ratios are consistent with previous measurements, we also note that the $^3_\Lambda\text{H}/^3\text{He}$ and $^3_{\overline{\Lambda}}\overline{\text{H}}/^3\overline{\text{He}}$ ratios in U + U and Au + Au collisions are lower than the previous STAR results[7] by 2.8σ and 1.9σ, respectively. We have investigated possible sources of the differences. The previous analysis used a mixture of minimum-bias and central triggered events. The ratios are expected to be higher in the central events[54,55]. The two analyses are also done in slightly different p_T ranges. These differences alone are not enough to explain the observed difference between the measured ratios at their face values.

Systematic uncertainties

Four main sources of systematic uncertainties are evaluated for the (anti)hypernucleus-lifetime measurements and the yield-ratio measurements: (1) systematic uncertainties on track-reconstruction efficiency, evaluated by varying the minimal number of measured points on the tracks; (2) systematic uncertainties on (anti)hypernucleus reconstruction efficiency due to topological selections, evaluated by varying the topological-selection viarables; (3) systematic uncertainties on (anti)hypernucleus signal-yield extraction from the invariant-mass spectra, evaluated by enlarging the invariant-mass ranges for signal-yield integration, and systematic uncertainties from the p_T-spectrum shapes, evaluated by narrowing the p_T-spectrum fit ranges; (4) systematic uncertainties on the (anti)helium yields, evaluated by varying the minimal number of measured points for $\langle \mathrm{d}E/\mathrm{d}x\rangle$ calculation and the cut on the helium-track DCA to primary vertex. The total systematic uncertainty is calculated as the quadratic sum of the four contributions above. The systematic uncertainty contributions from different sources for lifetime and yield-ratio measurements are summarized in Extended Data Tables 4–6. When calculating the yield

ratios, lifetimes and lifetime differences, the correlations of systematic uncertainties from the same sources have been considered. Thus, part of the systematic uncertainties will be cancelled.

Data availability

All raw data for this study were collected using the STAR detector at Brookhaven National Laboratory and are not available to the public. Derived data supporting the findings of this study are publicly available in the HEPData repository (https://www.hepdata.net/record/145132) or from the corresponding author on request.

Code availability

The codes to process raw data collected by the STAR detector are publicly available on GitHub[77] (https://github.com/star-bnl). The codes to analyse the produced data are not publicly available.

61. Llope, W. et al. The TOFp/pVPD time-of-flight system for STAR. *Nucl. Instrum. Methods Phys. Res. A* **522**, 252–273 (2004).
62. Adler, C. et al. The RHIC zero degree calorimeters. *Nucl. Instrum. Methods Phys. Res. A* **470**, 488–499 (2001).
63. Llope, W. JandS. T. A. Rcollaboration et al. Multigap RPCs in the STAR experiment at RHIC. *Nucl. Instrum. Methods Phys. Res. A* **661**, S110–S113 (2012).
64. Beddo, M. et al. The STAR Barrel Electromagnetic Calorimeter. *Nucl. Instrum. Methods Phys. Res. A* **499**, 725–739 (2003).
65. Anderson, M. et al. The STAR time projection chamber: a unique tool for studying high multiplicity events at RHIC. *Nucl. Instrum. Methods Phys. Res. A* **499**, 659–678 (2003).
66. Bichsel, H. A method to improve tracking and particle identification in TPCs and silicon detectors. *Nucl. Instrum. Methods Phys. Res. A* **562**, 154–197 (2006).
67. Kisel, I., Kulakov, I. & Zyzak, M. Standalone First Level Event Selection Package for the CBM Experiment. In *Proc. 18th Real-Time Conference (RT2012)* (2012).
68. Zyzak, M.*Online Selection of Short-lived Particles on Many-Core Computer Architectures in the CBM Experiment at FAIR*. PhD thesis, Johann Wolfgang Goethe-Universität (2016).
69. Ju, X.-Y. et al. Applying the Kalman filter particle method to strange and open charm hadron reconstruction in the STAR experiment. *Nucl. Sci. Tech.* **34**, 158 (2023).
70. Ablyazimov, T. O., Zyzak, M. V., Ivanov, V. V. & Kisel, P. I. Kalman filter-based fast track reconstruction for charged particles in a Compressed Baryonic Matter experiment using parallel computing on a multicore server at the Laboratory of Information Technologies, Joint Institute for Nuclear Research. *Phys. Part. Nucl. Lett.* **12**, 423–427 (2015).
71. Eckert, P., Achenbach, P. et al. Chart of hypernuclides – hypernuclear structure and decay data. https://hypernuclei.kph.uni-mainz.de (2023).
72. Cowan, G., Cranmer, K., Gross, E. & Vitells, O. Asymptotic formulae for likelihood-based tests of new physics. *Eur. Phys. J. C* **71**, 1554 (2011).
73. Brun, R., Bruyant, F., Maire, M., McPherson, A. C. & Zanarini, P. *GEANT3*. Report No. CERN-DD-EE-84-1 (CERN, 1987).
74. Fine, V. & Nevski, P. OO Model of STAR Detector for Simulation, Visualisation and Reconstruction. In *11th International Conference on Computing in High-Energy and Nuclear Physics*, 143–146 (2000).
75. Group, P. D. et al. Review of particle physics. *Prog. Theor. Exp. Phys.* **2022**, 083C01 (2022).
76. Schnedermann, E., Sollfrank, J. & Heinz, U. W. Thermal phenomenology of hadrons from 200 *A*/GeV S+S collisions. *Phys. Rev. C* **48**, 2462–2475 (1993).
77. STAR experiment at Relativistic Heavy Ion Collider. *GitHub*; https://github.com/star-bnl (2024).

Acknowledgements We thank the RHIC Operations Group and RCF at BNL, the NERSC Center at LBNL, and the Open Science Grid consortium for providing resources and support. This work was supported in part by the Office of Nuclear Physics within the US DOE Office of Science, the US National Science Foundation, National Natural Science Foundation of China, Chinese Academy of Science, the Ministry of Science and Technology of China and the Chinese Ministry of Education, the Higher Education Sprout Project by Ministry of Education at NCKU, the National Research Foundation of Korea, Czech Science Foundation and Ministry of Education, Youth and Sports of the Czech Republic, Hungarian National Research, Development and Innovation Office, New National Excellency Programme of the Hungarian Ministry of Human Capacities, Department of Atomic Energy and Department of Science and Technology of the Government of India, the National Science Centre and WUT ID-UB of Poland, the Ministry of Science, Education and Sports of the Republic of Croatia, German Bundesministerium für Bildung, Wissenschaft, Forschung and Technologie (BMBF), Helmholtz Association, Ministry of Education, Culture, Sports, Science, and Technology (MEXT), Japan Society for the Promotion of Science (JSPS) and Agencia Nacional de Investigación y Desarrollo (ANID) of Chile. We thank the Joint Department for Nuclear Physics, co-founded by the Lanzhou University and Institute of Modern Physics, Chinese Academy of Sciences, for the contributions of its students J. Wu and F. Zhao to this paper.

Author contributions All authors contributed to all research steps and writing of the paper.

Competing interests The authors declare no competing interests.

Additional information
Supplementary information The online version contains supplementary material available at https://doi.org/10.1038/s41586-024-07823-0.
Correspondence and requests for materials should be addressed to STAR Collaboration.
Peer review information *Nature* thanks Benjamin Dönigus and the other, anonymous, reviewer(s) for their contribution to the peer review of this work. Peer reviewer reports are available.

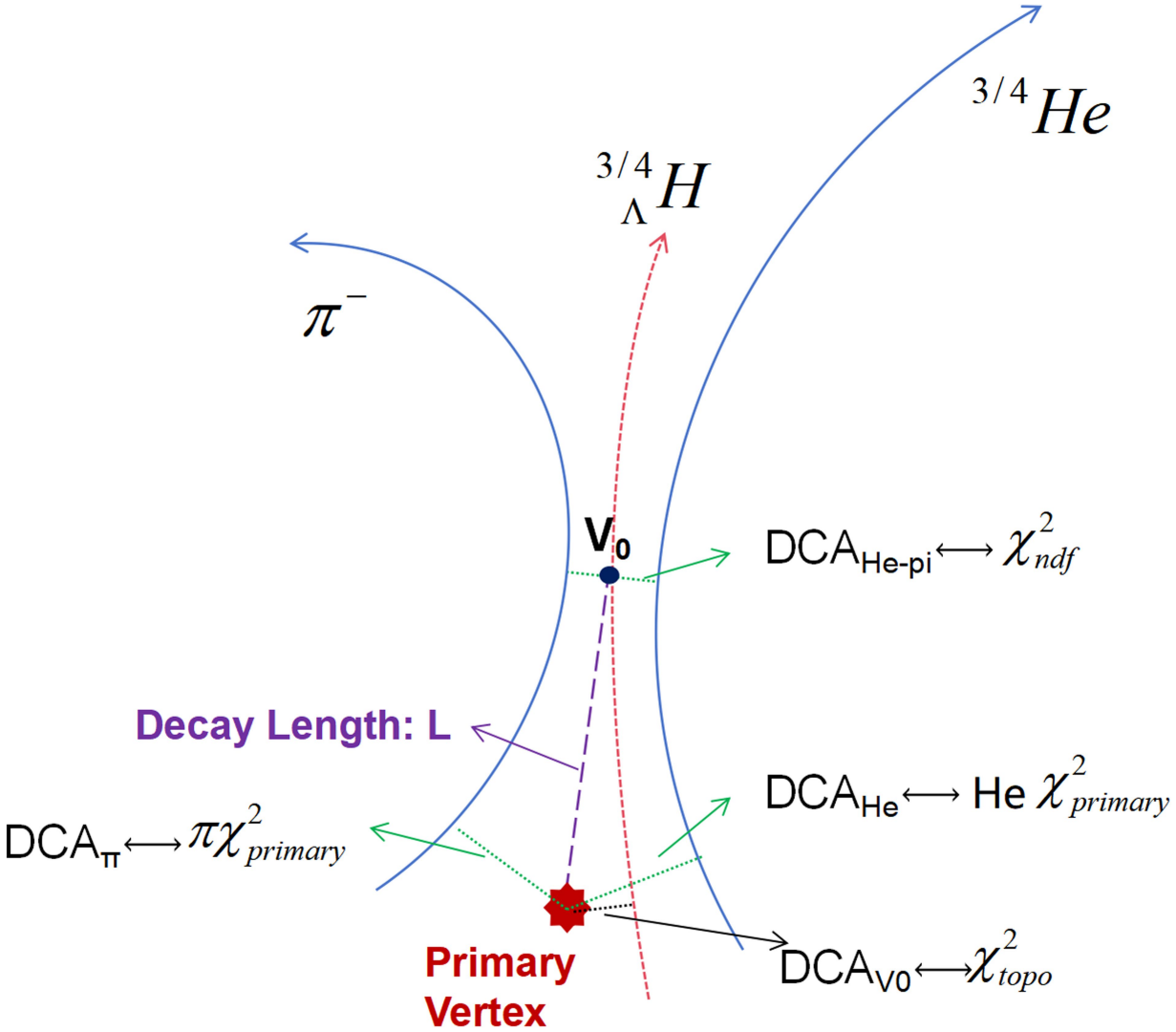

Extended Data Fig. 1 | Illustration of the decay topology of a hypernucleus and the variables for the selection criteria. The arrows indicate the relation between variables and their corresponding geometric distances.

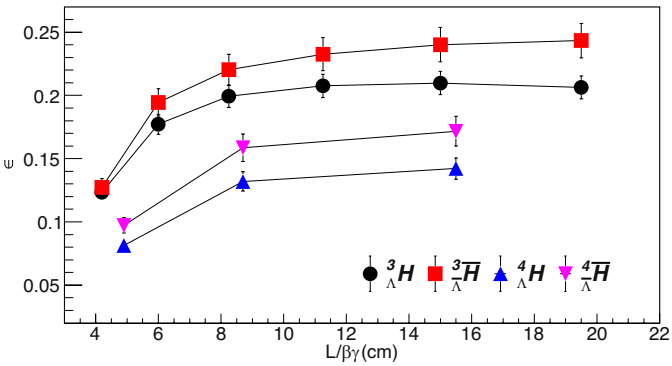

Extended Data Fig. 2 | Reconstruction efficiency as a function of $L/(\beta\gamma)$ obtained from the embedding Monte Carlo technique. Hypernuclei have stricter topological cuts than antihypernuclei to suppress knock-out ^{3}He and ^{4}He, resulting in lower efficiencies.

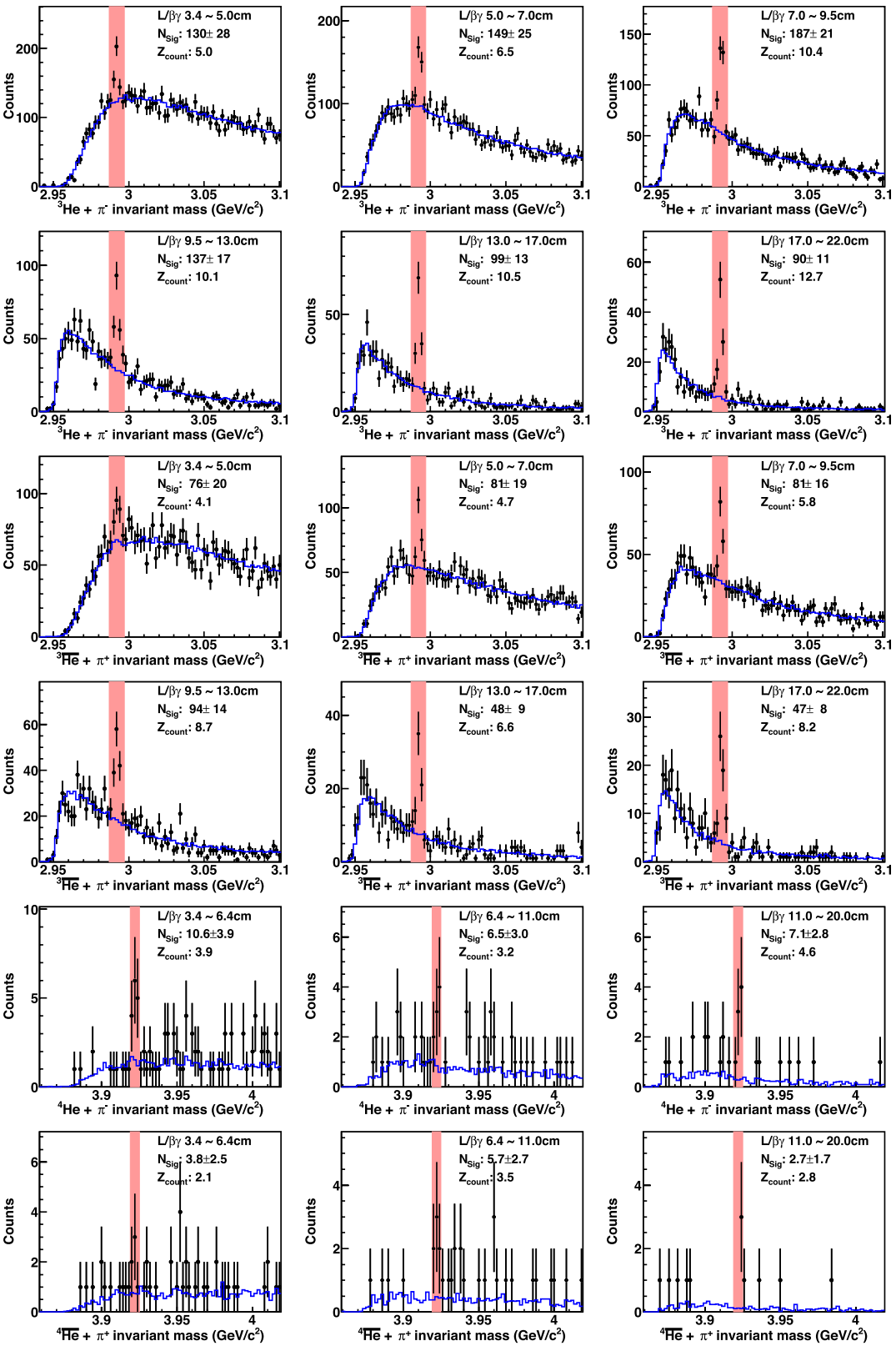

Extended Data Fig. 3 | $^3_\Lambda$H, $^3_{\overline{\Lambda}}\overline{\text{H}}$, $^4_\Lambda$H and $^4_{\overline{\Lambda}}\overline{\text{H}}$ candidate invariant-mass distributions in different $L/\beta\gamma$ intervals.

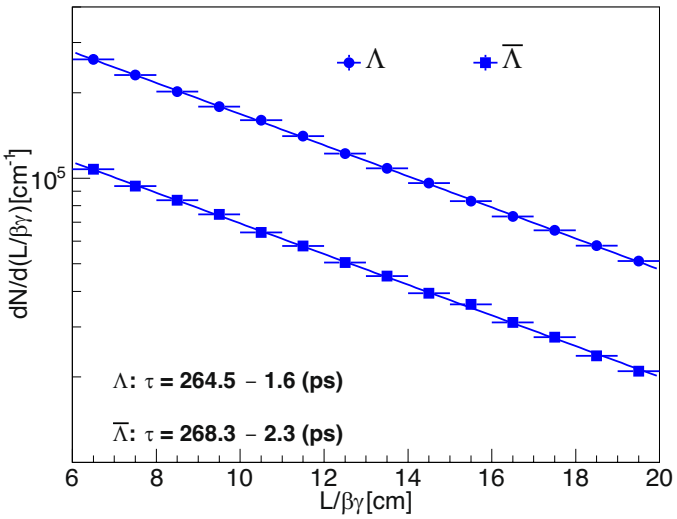

Extended Data Fig. 4 | $dN/d(L/\beta\gamma)$ as a function of $L/\beta\gamma$ for Λ and $\overline{\Lambda}$. The exponential fits are applied to obtain their lifetimes.

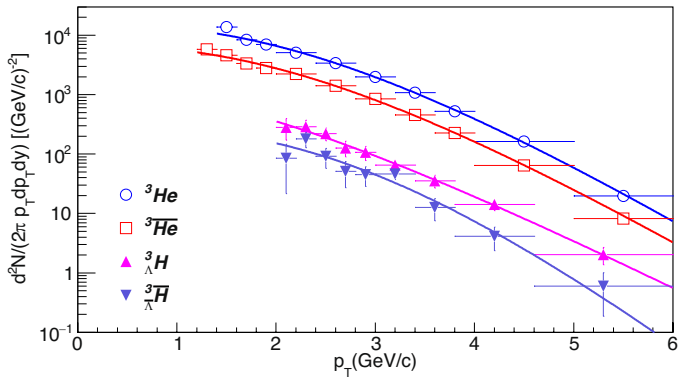

Extended Data Fig. 5 | Efficiency corrected p_T spectra for ^{3}He, $^3\overline{\text{He}}$, $^3_\Lambda$H, and $^3_\Lambda\overline{\text{H}}$. The spectra are in the phase space of $|y| < 0.7$ with only minimum-bias triggered events. The spectra are not normalized by the number of events. The lines represent the BW-function fits.

Extended Data Table 1 | Topological cuts for (anti)hypernucleus selection

Particles	χ^2_{topo}	χ^2_{NDF}	π $\chi^2_{primary}$	He $\chi^2_{primary}$	L(cm)	L/dL
${}^{3}_{\Lambda}\mathrm{H}$, ${}^{4}_{\Lambda}\mathrm{H}$	< 2	< 5	> 10	< 2000	> 3.5	> 3.4
${}^{3}_{\bar{\Lambda}}\overline{\mathrm{H}}$, ${}^{4}_{\bar{\Lambda}}\overline{\mathrm{H}}$	< 3	< 5	> 10	< 2000	> 3.5	> 3.4

Extended Data Table 2 | The signal and background counts in the measured phase space with minimum-bias triggered events

Collision systems		${}^{3}_{\Lambda}\mathrm{H}$	${}^{3}_{\bar{\Lambda}}\overline{\mathrm{H}}$	${}^{4}_{\Lambda}\mathrm{H}$	${}^{4}_{\bar{\Lambda}}\overline{\mathrm{H}}$
Total	N_{Sig}	606 ± 42	317 ± 31	13.3 ± 4.1	8.3 ± 3.3
	N_{Bg}	1145 ± 6	605 ± 5	3.9 ± 0.3	2.7 ± 0.3
Au+Au, U+U	N_{Sig}	207 ± 27	89 ± 19	-	-
	N_{Bg}	517 ± 5	267 ± 4	-	-
Zr+Zr, Ru+Ru	N_{Sig}	400 ± 32	228 ± 24	-	-
	N_{Bg}	627 ± 4	339 ± 3	-	-

Extended Data Table 3 | Fraction of (anti)helium nuclei from the two-body weak decays of (anti)hypernuclei in different collision systems

Collision systems	^{3}He	$^{3}\overline{\text{He}}$	^{4}He	$^{4}\overline{\text{He}}$
Total	(4.3±0.8)%	(4.9±1.1)%	(29±12)%	(42±21)%
Au+Au, U+U	(5.5±1.7)%	(6.2±2.5)%	-	-
Zr+Zr, Ru+Ru	(3.6±1.0)%	(4.0±1.5)%	-	-

The two-body decay branching fractions are assumed to be 0.25 for ${}^{3}_{\Lambda}$H and ${}^{3}_{\Lambda}\overline{\text{H}}$, 0.5 for ${}^{4}_{\Lambda}$H and ${}^{4}_{\Lambda}\overline{\text{H}}$.

Extended Data Table 4 | Systematic uncertainties on (anti)hypernucleus lifetimes

Sources	$\tau(^{3}_{\Lambda}\mathrm{H})$	$\tau(^{3}_{\bar{\Lambda}}\overline{\mathrm{H}})$	$\tau(^{4}_{\Lambda}\mathrm{H})$	$\tau(^{4}_{\bar{\Lambda}}\overline{\mathrm{H}})$
Track reconstruction	2.8%	8.9%	15.5%	16.8%
Topological selection	4.5%	7.3%	11.9%	10.5%
Signal extraction & p_T shape	0.4%	0.5%	2.4%	3.8%
Total	5.4%	11.6%	19.7%	20.1%

Extended Data Table 5 | Systematic uncertainties on yield ratios in all measured collision systems

Sources	$\frac{^3\overline{\mathrm{He}}}{^3\mathrm{He}}$	$\frac{^4\overline{\mathrm{He}}}{^4\mathrm{He}}$	$\frac{^3_{\overline{\Lambda}}\overline{\mathrm{H}}}{^3_{\Lambda}\mathrm{H}}$	$\frac{^4_{\overline{\Lambda}}\overline{\mathrm{H}}}{^4_{\Lambda}\mathrm{H}}$	$\frac{^3_{\Lambda}\mathrm{H}}{^3\mathrm{He}}$	$\frac{^4_{\Lambda}\mathrm{H}}{^4\mathrm{He}}$	$\frac{^3_{\overline{\Lambda}}\overline{\mathrm{H}}}{^3\overline{\mathrm{He}}}$	$\frac{^4_{\overline{\Lambda}}\overline{\mathrm{H}}}{^4\overline{\mathrm{He}}}$
Track reconstruction	0.6%	0.6%	12.6%	12.6%	5.8%	5.8%	10.8%	10.8%
Topological selection	0.6%	0.6%	11.4%	11.4%	3.8%	3.8%	13.7%	13.7%
Signal extraction & p_T shape	0.1%	22.2%	1.9%	46.3%	6.0%	20.4%	8.2%	49.9%
(Anti)helium yields	0.3%	0.3%	-	-	3.4%	3.4%	3.2%	3.2%
Total	0.9%	22.2%	17.1%	49.3%	9.8%	21.8%	19.5%	52.9%

Extended Data Table 6 | Systematic uncertainties on yield ratios in big and small collision systems

	Au+Au, U+U		Zr+Zr, Ru+Ru	
Sources	$\frac{^3_\Lambda\mathrm{H}}{^3\mathrm{He}}$	$\frac{^3_{\bar{\Lambda}}\overline{\mathrm{H}}}{^3\overline{\mathrm{He}}}$	$\frac{^3_\Lambda\mathrm{H}}{^3\mathrm{He}}$	$\frac{^3_{\bar{\Lambda}}\overline{\mathrm{H}}}{^3\overline{\mathrm{He}}}$
Track reconstruction	8.1%	27.0%	3.6%	4.9%
Topological selection	7.0%	28.9%	3.7%	7.9%
Signal extraction & p_T shape	15.1%	18.3%	3.0%	0.6%
(Anti)helium yields	4.2%	3.5%	3.8%	1.9%
Total	19.0%	43.7%	7.1%	9.5%